

Vector dc magnetic-field sensing with a reference microwave field using perfectly aligned nitrogen-vacancy centers in diamond

Takuya Isogawa^{1,*}, Yuichiro Matsuzaki^{2,†} and Junko Ishi-Hayase^{1,‡}

¹*Department of Applied Physics and Physico-Informatics, Keio University, Yokohama 223-8522, Japan*

²*National Institute of Advanced Industrial Science and Technology, Ibaraki 305-8568, Japan*



(Received 13 December 2021; accepted 14 June 2023; published 29 June 2023)

The measurement of vector magnetic fields with high sensitivity and spatial resolution is important for both fundamental science and engineering applications. In particular, magnetic-field sensing with nitrogen-vacancy (NV) centers in diamond is a promising approach that can outperform existing methods. Recent studies have demonstrated vector dc magnetic-field sensing with perfectly aligned NV centers, which showed a higher readout contrast than NV centers having four equally distributed orientations. However, to estimate the azimuthal angle of the target magnetic field with respect to the NV axis in these previous approaches, it is necessary to apply a strong reference dc magnetic field, which can perturb the system to be measured. This is a crucial problem, especially when attempting to measure vector magnetic fields from materials that are sensitive to applied dc magnetic fields. Here, we propose a method to measure vector dc magnetic fields using perfectly aligned NV centers without reference dc magnetic fields. This method can be performed even with a single NV center. More specifically, we use the direction of linearly polarized microwave fields to induce Rabi oscillation as a reference and we estimate the azimuthal angle of the target fields from the Rabi frequency. We further demonstrate the potential of our method to improve sensitivity by using entangled states to overcome the standard quantum limit. Our method of using a reference microwave field is an alternative technique for sensitive vector dc magnetic-field sensing.

DOI: [10.1103/PhysRevA.107.062423](https://doi.org/10.1103/PhysRevA.107.062423)

I. INTRODUCTION

The detection of dc magnetic fields on the nanoscale plays an essential role in a wide range of fields, from biology to condensed-matter physics [1,2]. Substantial effort has been devoted to the development of devices for measuring small magnetic fields in a local region [3–6]. The electron spin in the nitrogen-vacancy (NV) center in diamond is known to be sensitive to magnetic fields, and it combines the advantages of noninvasiveness, high sensitivity, and nanoscale resolution [7–10]. The NV center is a spin-1 system, and the frequencies of the ground-state manifolds can be shifted by magnetic fields. Vector magnetic-field sensing with NV centers has been attracting much attention [11–16]. It has a variety of potential applications, including the imaging of living cells [17], mapping of current distribution [18–21], and reconstruction of vector magnetic fields from ferromagnetic materials [22,23].

The sensing of dc magnetic fields is conventionally performed using Ramsey interferometry or optically detected magnetic resonance (ODMR) [24,25]. Using different NV

orientations, the vector components of the magnetic field along each quantization axis can be used to reconstruct dc or ac vector fields [11,13]. However, one drawback of these methods is the reduction of the fluorescence contrast. The contrast decreases by a factor of 4 compared to that of a single NV, which degrades the sensitivity. Multifrequency control of the NV centers has been proposed and demonstrated as a solution to this problem, but complex microwave pulse sequences are required to implement these schemes [26–29]. For more practical applications, previous studies have devised an ingenious method of measuring vector magnetic fields using a single NV center or perfectly aligned NV centers [30–36]. It is known that the longitudinal and transverse components of the target vector dc magnetic fields are estimated from the shifts in frequencies of the transitions between ground-state manifolds [9], whereas a reference dc field is used to estimate the azimuthal angle of the target field with respect to the NV axis [31,35]. However, the reference dc field can be invasive when measuring the magnetic properties of ferromagnets and superconductors that are sensitive to dc magnetic fields. Therefore, it is desirable to measure the azimuthal angle without a reference dc field for the investigation of various phenomena of magnetic-field-sensitive materials [22,23,37,38].

In this study, we propose a scheme to measure the azimuthal angle of the target magnetic field without using a reference dc field. In our scheme, the azimuthal angle of the target magnetic field can be estimated from the Rabi frequency using the direction of linearly polarized microwave fields as a reference. The transverse component of the dc field changes the direction of the quantization axis of the NV center.

*Current address: Department of Nuclear Science and Engineering, Massachusetts Institute of Technology, Cambridge, Massachusetts 02139, USA; isogawa@mit.edu; tisogawa@keio.jp

†Current address: Department of Electrical, Electronic, and Communication Engineering, Chuo University, Bunkyo-ku, Tokyo 112-8551, Japan; ymatsuzaki872@g.chuo-u.ac.jp; matsuzaki.yuichiro@aist.go.jp

‡hayase@appi.keio.ac.jp

On the other hand, when we apply the resonant microwave field, only the component perpendicular to the quantization axis contributes to the change in the Rabi frequency [39]. Thus, the change in the direction of the quantization axis can be estimated from the Rabi frequency, and thus, the direction of the dc magnetic field can be measured. Similar to the previous methods, our method can be performed with a single NV center, which improves the spatial resolution. Our scheme provides a practical approach to achieve full vector dc magnetometry without additional reference dc fields using a single NV center or a perfectly aligned ensemble of NV centers.

In addition, by using perfectly aligned NV centers, we investigate whether the use of entanglement improves the sensitivity of our scheme. By using an entangled state with L spins to measure magnetic fields, the uncertainty of the estimation decreases by $1/L$, which is called the Heisenberg limit, under ideal conditions, while the uncertainty decreases by $1/\sqrt{L}$ with L separable spins, which is called the standard quantum limit (SQL) [40,41]. However, because the quantum state is fragile against decoherence, it is unclear whether the entangled sensor shows sensitivity better than that of the classical one. For certain types of noise, the entangled states can outperform the SQL [42–46]. In our case, the NV centers are affected by magnetic-field noise. Contrary to the conventional belief that entanglement provides no advantage over separable states in standard Ramsey interferometry in the presence of Markovian dephasing [40], our scheme is one of the cases where this is not the case. Therefore, we investigate the performance of the entanglement sensor in estimating the azimuthal angle with magnetic noise in our scheme. Furthermore, we numerically show that our sensing scheme with entanglement has sensitivity better than that of separable sensors, even under the effect of noise.

The remainder of this paper is organized as follows. In Sec. II, we review the conventional vector magnetic-field sensing scheme with standard Ramsey interference using a reference dc magnetic field. In Sec. III, we explain our scheme of vector magnetic-field sensing with Rabi oscillation using a reference microwave field. In Sec. IV, we discuss the sensitivity of our scheme and investigate the potential improvement when using entangled states. Finally, Sec. V concludes the paper.

II. CONVENTIONAL SCHEME

A. Measurement of longitudinal and transverse components of target magnetic fields

Here, we review a conventional scheme that measures the longitudinal and transverse components of target magnetic fields. The Hamiltonian of the NV center is given as

$$H_0 = D\hat{S}_z^2 + \gamma_e B_z \hat{S}_z + \gamma_e B_\perp (\cos \phi_s \hat{S}_x + \sin \phi_s \hat{S}_y), \quad (1)$$

where $D = 2\pi \times 2.87$ GHz is the zero-field splitting, $\gamma_e = 2\pi \times 28$ GHz/T is the gyromagnetic ratio, $\{\hat{S}_x, \hat{S}_y, \hat{S}_z\}$ are the spin-1 operators, and $\{B_z, B_\perp, \phi_s\}$ are the local magnetic-field components in cylindrical coordinates. Throughout this paper, we assume that $\hbar = 1$. Following Refs. [9,35], we consider the characteristic equation given by

$$(D - x)^2 x + \frac{1}{2} \gamma_e^2 B^2 [D(1 - \cos 2\theta) - 2x] = 0, \quad (2)$$

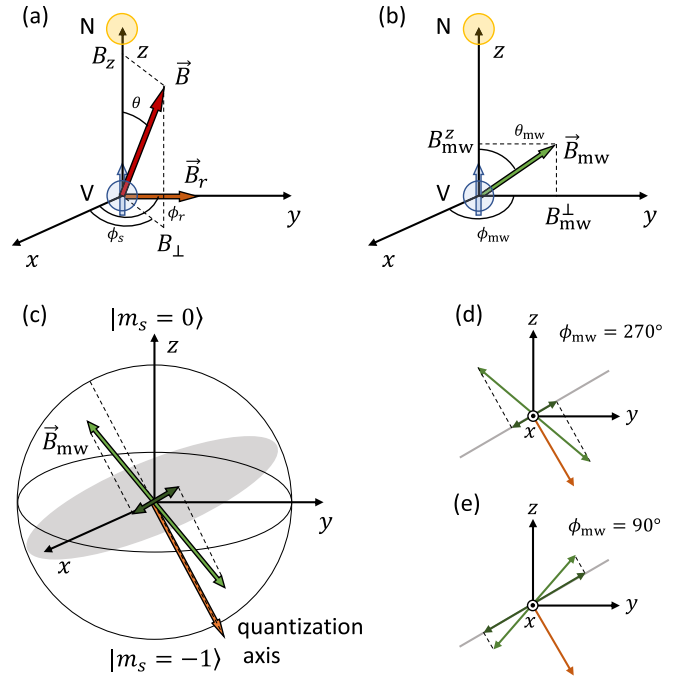


FIG. 1. Schematic of our vector dc magnetic-field sensing scheme. In panel (a), we show a configuration of the NV axis, the target vector magnetic field, and the reference dc magnetic field. In panel (b), we show a configuration of the NV axis and the reference microwave field. In panel (c), relations between the quantization axis and the direction of the microwave fields in a Bloch sphere are illustrated. In panels (d) and (e), we show the Bloch sphere projected onto the y and z planes at $\phi_{mw} = 270^\circ$ and $\phi_{mw} = 90^\circ$, respectively, with $\phi_s = 90^\circ$.

where $\theta = \arctan(B_\perp/B_z)$, $B = \sqrt{B_s^2 + B_\perp^2}$, and x denotes the eigenenergy of the Hamiltonian. If we express the frequency of the ground state as x_0 , the frequencies of the other energy eigenstates can be expressed as $x_+ = x_0 + \omega_+$ and $x_- = x_0 + \omega_-$. By substituting these expressions into Eq. (2), we obtain the following equations:

$$x_0 = \frac{1}{3}(2D - \omega_+ - \omega_-), \quad (3)$$

$$B = \sqrt{\frac{1}{3\gamma_e^2}(\omega_+^2 + \omega_-^2 - \omega_+\omega_- - D^2)}, \quad (4)$$

$$\sin \theta = \sqrt{\frac{-x_0^3 + 2Dx_0^2 + (\gamma_e^2 B^2 - D^2)x_0}{D\gamma_e^2 B^2}}. \quad (5)$$

Thus, from the transition frequencies ω_\pm , which can be measured by Ramsey interferometry or ODMR, we can determine the longitudinal and transverse components of the target magnetic fields.

B. Measurement of the azimuthal angle of the target fields

Next, we review a conventional scheme that measures the azimuthal angle of the target magnetic field using a dc magnetic field as a reference [Fig. 1(a)]. By applying a reference magnetic field with known amplitude and direction, we can determine the azimuthal angle of the target magnetic field

from the change in resonant frequency of the NV centers. The frequency shift can be measured via Ramsey interferometry.

Our goal here is to determine the azimuthal angle ϕ_s . When we apply a reference dc magnetic field perpendicular to the NV axis, an additional term,

$$H_r = \gamma_e B_r (\cos \phi_r \hat{S}_x + \sin \phi_r \hat{S}_y), \quad (6)$$

is added to the system Hamiltonian, where B_r and ϕ_r are the amplitude and the azimuthal angle of the reference field, respectively. This allows us to measure the change in transition frequency between the ground state $|g\rangle \simeq |m_s = 0\rangle$ and another energy eigenstate. By using the perturbation theory for small $\gamma_e B_{\text{tot}}/D$, such transitions frequencies are approximately given by [47]

$$\omega_{\pm} \simeq D \pm \gamma_e B_z + \frac{3(\gamma_e B_{\perp}')^2}{2D}, \quad (7)$$

where $B_{\perp}' = \sqrt{B_{\perp}^2 + B_r^2 + 2B_{\perp}B_r \cos(\phi_s - \phi_r)}$ and $B_{\text{tot}} = \sqrt{B_s^2 + B_{\perp}'^2}$. We consider the subspace spanned by $|g\rangle$ and the first excited state $|e\rangle$ and define $\Delta = D - \gamma_e B_z$. In a rotating frame defined by $U = \exp(-i\Delta \hat{S}_z t)$, the effective Hamiltonian of this subspace is given by

$$H_{\text{eff}}^{(\text{dc})} = \frac{\delta\omega}{2} (|e\rangle\langle e| - |g\rangle\langle g|), \quad (8)$$

where $\delta\omega = 3(\gamma_e B_{\perp}')^2/2D$ is the frequency shift. We create a superposition $|+\rangle = (|e\rangle + |g\rangle)/\sqrt{2}$ by using a $\pi/2$ pulse, and a relative phase can be accumulated during the interaction time t . Then, we perform a projective measurement on

$|+\rangle$ with a probability of $P = [1 + \cos(\delta\omega t)]/2$, which can be constructed using a $\pi/2$ pulse and a subsequent optical readout. Thus, we can estimate ϕ_s by sweeping ϕ_r via the Ramsey scheme.

III. OUR SCHEME

Here, we explain our scheme for measuring the azimuthal angles of the target fields without reference dc magnetic fields. In analogy to the conventional method using the dc magnetic field as a reference, we apply the reference microwave field, the amplitude and the direction of which are known [Fig. 1(b)]. The azimuthal angle of the target magnetic field can be estimated by measuring the Rabi oscillations caused by the reference microwave field.

To illustrate our idea, we start with a simple model by considering a subspace spanned by $|m_s = 0\rangle$ and $|m_s = -1\rangle$, which we call the qubit approximation. The Hamiltonian for this subspace is

$$H_0^{(1/2)} = -\frac{\Delta}{2} \hat{\sigma}_z + \frac{\gamma_e B_{\perp}}{\sqrt{2}} (\cos \phi_s \hat{\sigma}_x + \sin \phi_s \hat{\sigma}_y), \quad (9)$$

where $\{\hat{\sigma}_x, \hat{\sigma}_y, \hat{\sigma}_z\}$ are the Pauli matrices. The quantization axis is along the direction $(\frac{\gamma_e B_{\perp}}{\sqrt{2}} \cos \phi_s, \frac{\gamma_e B_{\perp}}{\sqrt{2}} \sin \phi_s, -\frac{\Delta}{2})$. Any state of a two-level system can be represented by a Bloch sphere [Fig. 1(c)]. By diagonalizing $H_0^{(1/2)}$, we have $H_0^{(1/2)} = \omega^{(1/2)} (|g^{(1/2)}\rangle\langle g^{(1/2)}| - |e^{(1/2)}\rangle\langle e^{(1/2)}|)/2$, where

$$\omega^{(1/2)} = \sqrt{\Delta^2 + 2\gamma_e^2 B_{\perp}^2}, \quad (10)$$

and

$$|g^{(1/2)}\rangle = c_g \left(\frac{e^{-i\phi_s} (\Delta + \sqrt{\Delta^2 + 2\gamma_e^2 B_{\perp}^2})}{\sqrt{2}\gamma_e B_{\perp}} |m_s = 0\rangle + |m_s = -1\rangle \right),$$

$$|e^{(1/2)}\rangle = c_e \left(\frac{e^{-i\phi_s} (\Delta - \sqrt{\Delta^2 + 2\gamma_e^2 B_{\perp}^2})}{\sqrt{2}\gamma_e B_{\perp}} |m_s = 0\rangle + |m_s = -1\rangle \right)$$

are the eigenstates. Here, c_g and c_e denote normalization constants. When the dc field is applied in a direction different from that of the NV axis, the quantization axis is slightly tilted owing to the perpendicular component of the dc field. Let us consider the Hamiltonian when we apply the microwave field. The Hamiltonian becomes $H^{(1/2)} = H_0^{(1/2)} + H_{\text{mw}}^{(1/2)}$, where $H_{\text{mw}}^{(1/2)}$ is the driving microwave Hamiltonian expressed as

$$H_{\text{mw}}^{(1/2)} = \left(\frac{\gamma_e B_{\text{mw}}^z}{2} \hat{\sigma}_z + \frac{\gamma_e B_{\text{mw}}^{\perp}}{\sqrt{2}} (\cos \phi_{\text{mw}} \hat{\sigma}_x + \sin \phi_{\text{mw}} \hat{\sigma}_y) \right) \cos \omega^{(1/2)} t, \quad (11)$$

and we define $\theta_{\text{mw}} = \arctan(B_{\text{mw}}^{\perp}/B_{\text{mw}}^z)$. In a rotating frame defined by $U = \exp(-iH_0^{(1/2)} t)$, the effective Hamiltonian is

$$H_{\text{eff}}^{(1/2)} = \frac{1}{2} (\Omega |g^{(1/2)}\rangle\langle e^{(1/2)}| + \Omega^* |e^{(1/2)}\rangle\langle g^{(1/2)}|), \quad (12)$$

where

$$\lambda = |\Omega| = c_g c_e \left| -\gamma_e B_{\text{mw}}^z + \frac{\Delta}{B_{\perp}} B_{\text{mw}}^{\perp} [\cos(\phi_s - \phi_{\text{mw}}) + i\sqrt{1 + 2(\gamma_e B_{\perp}/\Delta)^2} \sin(\phi_s - \phi_{\text{mw}})] \right| \quad (13)$$

is the Rabi frequency between $|g^{(1/2)}\rangle$ and $|e^{(1/2)}\rangle$. Here, we used rotating-wave approximation (RWA). We plot λ of Eq. (13) against $\phi = \phi_s - \phi_{\text{mw}}$ in Fig. 2 (orange dashed

curve). Because λ is given by the absolute value of a complex number, we can interpret this as the distance from the origin of the complex plane (Fig. 3). On the complex

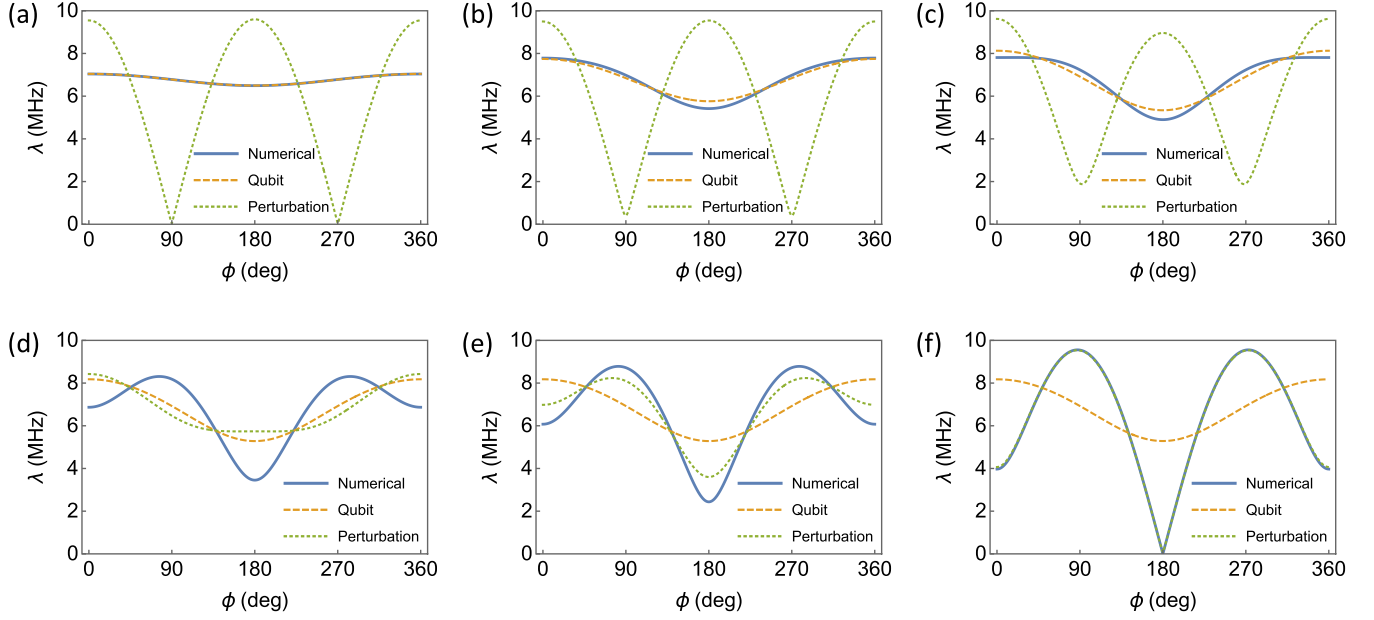


FIG. 2. Rabi frequency as a function of the azimuthal angle ϕ between the target magnetic field of $B = 8$ mT and the driving microwave field of $B_{\text{mw}} = 1$ mT. We set the polar angle of the microwave fields as $\theta_{\text{mw}} = 20^\circ$. The polar angles of the target field θ are (a) 10° , (b) 40° , (c) 70° , (d) 85° , (e) 87° , and (f) 89° . We use the numerical (blue solid curve), qubit-approximation (orange dashed curve), and perturbation (green dotted curve) values, given by Eqs. (16), (13), and (18), respectively.

plane, λ is the distance between the origin and a point on an ellipse having a width, height, and center of $c_g c_e \Delta B_{\text{mw}}^\perp / B_\perp$, $c_g c_e (\Delta B_{\text{mw}}^\perp / B_\perp) \sqrt{1 + 2(\gamma_e B_\perp / \Delta)^2}$, and $(c_g c_e \gamma_e B_{\text{mw}}^z, 0)$,

respectively [Fig. 3(b)]. Because $2(\gamma_e B_\perp / \Delta)^2 \ll 1$, the ellipse is close to a circle. If B_{mw}^z is sufficiently large, the change in λ also becomes large, resulting in better sensitivity. This results from the fact that, in the Bloch-sphere description, the Rabi frequency is proportional to the microwave component perpendicular to the quantization axis.

We illustrate this point in Fig. 1. This shows the case when the azimuthal angles of the quantization axis are equal to [see Fig. 1(d)] or equal but opposite in sign to [see Fig. 1(e)] that of the applied-microwave-field direction. As can be observed from geometrical interpretation, when the azimuthal angles of the quantization axis and the microwave field are equal (equal but opposite in sign), the component of the microwave perpendicular to the quantization axis is minimized (maximized).

Let us consider a more general model: The spin-1 Hamiltonian. We define $|g\rangle$ and $|e\rangle$ as the ground state and the first excited state of the Hamiltonian H_0 . When a resonant microwave is applied, the Hamiltonian becomes $H = H_0 + H_{\text{mw}}$, where H_{mw} is the driving microwave Hamiltonian,

$$H_{\text{mw}} = \gamma_e \vec{B}_{\text{mw}} \cdot \vec{S} \cos \omega_- t, \quad (14)$$

$$\vec{B}_{\text{mw}} = (B_{\text{mw}}^z, B_{\text{mw}}^\perp \cos \phi_{\text{mw}}, B_{\text{mw}}^\perp \sin \phi_{\text{mw}}).$$

In a rotating frame defined by $U = \exp(-iH_0 t)$, the effective Hamiltonian is

$$H_{\text{eff}}^{(\text{mw})} = \frac{1}{2}(\Omega|g\rangle\langle e| + \Omega^*|e\rangle\langle g|), \quad (15)$$

where

$$\lambda = |\Omega| = |\langle g|\gamma_e \vec{B}_{\text{mw}} \cdot \vec{S}|e\rangle| \quad (16)$$

is the Rabi frequency between $|g\rangle$ and $|e\rangle$. Here, we have used the RWA. We cannot obtain a simple analytical form of the eigenstates of H_0 . Instead, we perform numerical simulations to calculate the Rabi frequency in Fig. 2 (blue solid curve) and

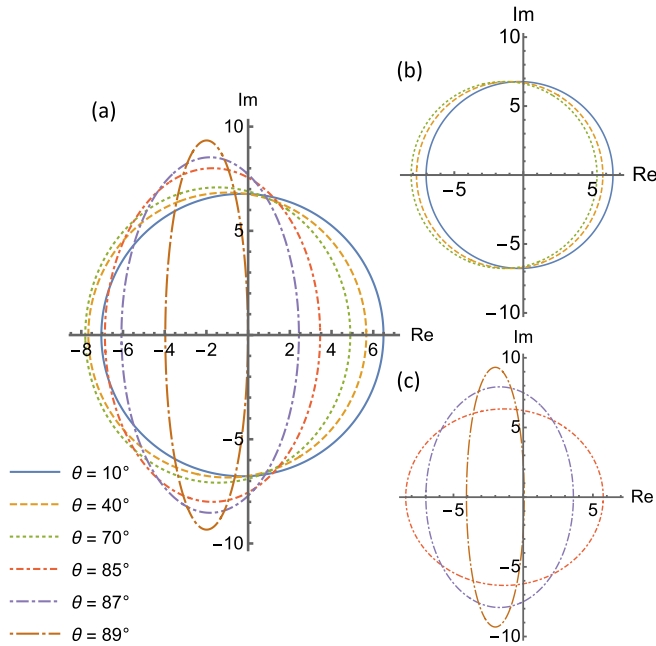


FIG. 3. Plot of $\langle g|\gamma_e \vec{B}_{\text{mw}} \cdot \vec{S}|e\rangle$ in Eq. (16) on the complex plane. Each ellipse is obtained by sweeping the azimuthal angle ϕ between the target magnetic field and the driving microwave field. The parameters are the same as those used in Fig. 2. In panel (a), we numerically plot $\langle g|\gamma_e \vec{B}_{\text{mw}} \cdot \vec{S}|e\rangle$ without approximations. In panel (b), we use the qubit approximation. In panel (c), we use the perturbation theory described in Eq. (17).

Fig. 3(a). As can be observed in Fig. 2, when θ approaches 90° , the difference between the results with numerical simulations and those with qubit approximations becomes more pronounced because the eigenstates become superpositions of all three states.

To understand this point, we use perturbation theory to calculate the Rabi frequency under the assumption that D and B_\perp are much larger than B_z . In this case, the eigenstates of the Hamiltonian are expressed as $|g\rangle \simeq |m_s = 0\rangle - \epsilon|B\rangle$, $|d\rangle = |D\rangle$, and $|b\rangle \simeq |B\rangle + \epsilon|m_s = 0\rangle$, where $\epsilon = \gamma_e B_\perp / D$, $|B\rangle = (|m_s = +1\rangle + |m_s = -1\rangle) / \sqrt{2}$, and $|D\rangle = (|m_s = +1\rangle - |m_s = -1\rangle) / \sqrt{2}$. We call $|B\rangle$ ($|D\rangle$) a bright (dark) state. This representation is particularly useful when we apply a magnetic field orthogonal to the NV axis or electric (strain) fields [48–51]. The first-order corrections to $|g\rangle$ and $|d\rangle$ are

$$|g^{(1)}\rangle = c_{gd}|d\rangle, \quad |d^{(1)}\rangle = c_{dg}|g\rangle + c_{db}|b\rangle, \\ c_{gd} = -c_{dg} = -\frac{\epsilon\gamma_e B_z}{D + \epsilon\gamma_e B_\perp}, \quad c_{db} = -\frac{B_z}{\epsilon B_\perp}, \quad (17)$$

which allow us to obtain the Rabi frequency between $|g'\rangle = c_{g'}(|d\rangle + |d^{(1)}\rangle)$ and $|d'\rangle = c_{d'}(|g\rangle + |g^{(1)}\rangle)$,

$$|\langle d'|H_{\text{mw}}|g'\rangle| \simeq c_{g'}c_{d'}| -\epsilon\gamma_e B_{\text{mw}}^z + \gamma_e B_{\text{mw}}^\perp [c_{db} \cos(\phi_s - \phi_{\text{mw}}) + i \sin(\phi_s - \phi_{\text{mw}})]|, \quad (18)$$

where $c_{g'}$ and $c_{d'}$ are normalization constants. Here as well, we have used the RWA. We also plot $|\langle d'|H_{\text{mw}}|g'\rangle|$ of Eq. (18) against $\phi = \phi_s - \phi_{\text{mw}}$ in Fig. 2 (green dotted curve). As in the case of the qubit system approximation, we can interpret this as a distance on the complex plane (Fig. 3). In this case, the width, height, and center of the ellipse are $c_{g'}c_{d'}c_{db}\gamma_e B_{\text{mw}}^\perp$, $c_{g'}c_{d'}\gamma_e B_{\text{mw}}^\perp$, and $(-c_{g'}c_{d'}\epsilon\gamma_e B_{\text{mw}}^z, 0)$, respectively. Because $\epsilon, c_{db} \ll 1$, the ellipse has a long, narrow shape [Fig. 3(c)]. Thus, λ is maximized when the point on the ellipse is located at either the top or the bottom of the ellipse, that is, $\phi_s - \phi_{\text{mw}} = 90^\circ$ and 270° .

The Rabi oscillation can be probed by measuring the population of $|g\rangle$ with the probability $P = [1 + \cos(\lambda t)]/2$. Thus, we can estimate ϕ_s by sweeping ϕ_{mw} via the measurement of Rabi frequencies.

IV. SENSITIVITY

A. Separable states

In this section, we calculate the uncertainty of estimation of our scheme and make a comparison with the conventional scheme. Although our scheme has the qualitative advantage of not using the reference dc field, we show that, in some cases, the sensitivity of our scheme is comparable to or better than that of the conventional scheme.

If we have an approximate value of the azimuthal angle ϕ_s , we can rewrite it as $\phi_s = \phi_a + \phi'$, where ϕ_a is the approximate value and ϕ' is a small difference from the true value. The Rabi frequency is then given by $\lambda = \lambda_a + \lambda'$, where λ_a is the approximate value and λ' is a small difference from the true value. We can adjust the interaction time as

$$\tau = \frac{(2n-1)\pi}{2\lambda_a}, \quad (19)$$

and we obtain $P \simeq (1 + \lambda'\tau)/2$, where we assume $\lambda'\tau \ll 1$. By repeating this experiment many times, we can obtain the probability from the experimental results; thus, the value of ϕ_s and λ can be estimated.

The uncertainty of the estimation is given by

$$\delta\phi = \frac{\sqrt{P(1-P)}}{\left|\frac{dP}{d\phi}\right|\sqrt{N}}, \quad (20)$$

where N is the number of repetitions of the experiment and $\phi = \phi_s - \phi_{\text{mw}}$ denotes the azimuthal angle to be estimated. We assume that the interaction time τ is much longer than the state preparation time and the measurement readout time. In this case, we have $N \simeq T/\tau$, where T is a given time for the sensing. We can calculate the uncertainty as

$$\delta\phi \simeq \frac{1}{\left|\frac{d\lambda}{d\phi}\right|\sqrt{T\tau}}. \quad (21)$$

Now, we consider the magnetic-field sensing under the effect of decoherence. The dominant noise is due to small fluctuations in the magnetic field due to nitrogen impurities or environmental nuclear spins, which lead to fluctuations in the energy splitting [52]. With $D \gg \gamma_e B$, the noise from B_\perp is suppressed by a large D and becomes negligible as compared to B_z , as expressed in Eq. (7). Thus, the effect of decoherence can be described by the standard Lindblad-type master equation:

$$\frac{d\rho(t)}{dt} = -i[H_{\text{eff}}, \rho(t)] - \Gamma[\hat{S}_z, [\hat{S}_z, \rho(t)]], \quad (22)$$

where Γ is the decay rate. In this case, the probability of projecting the state onto $|g\rangle$ can be calculated as $P = \text{Tr}[|g\rangle\langle g|\rho(t)]$. We numerically calculate the probability P with the initial state $\rho(0) = |g\rangle\langle g|$, and we observe a linear dependence of the probability on a small λ' for B_\perp between 0.1 and 10 mT. The probability P is, thus, expressed as

$$P \simeq \frac{1}{2}(1 + c_{\tau,\Gamma}\lambda'), \quad (23)$$

where the factor $c_{\tau,\Gamma}$ represents the signal decay, and we can numerically calculate this factor. By substituting Eq. (23) into Eq. (20), we obtain the uncertainty of the estimation:

$$\delta\phi \simeq \frac{1}{c_{\tau,\Gamma}\left|\frac{d\lambda}{d\phi}\right|\sqrt{T/\tau}}. \quad (24)$$

We can calculate the uncertainty for the conventional scheme in a way similar to that for our scheme, and we obtain $\delta\phi \simeq 1/c_{\tau,\Gamma}\left|\frac{d\delta\omega}{d\phi}\right|\sqrt{T/\tau}$ (see a derivation in Appendix A). Thus, to compare the performance of our method with that of the conventional method, we need to calculate $c_{\tau,\Gamma}$, $c_{\tau,\Gamma}'$, $\left|\frac{d\lambda}{d\phi}\right|$, and $\left|\frac{d\delta\omega}{d\phi}\right|$.

First, we performed numerical simulations to calculate $\left|\frac{d\lambda}{d\phi}\right|$ and $\left|\frac{d\delta\omega}{d\phi}\right|$, as shown in Fig. 4. When the reference field is parallel to the target field, both λ and $\delta\omega$ reach a local maximum or minimum, and the uncertainty $\delta\phi$ tends to infinity at these points. As can be observed in Figs. 4(a) and 4(b), when B_{mw} is comparable to B_r , $\left|\frac{d\lambda}{d\phi}\right|$ is of the same order of magnitude as $\left|\frac{d\delta\omega}{d\phi}\right|$. Let us consider a case with a small amplitude of the

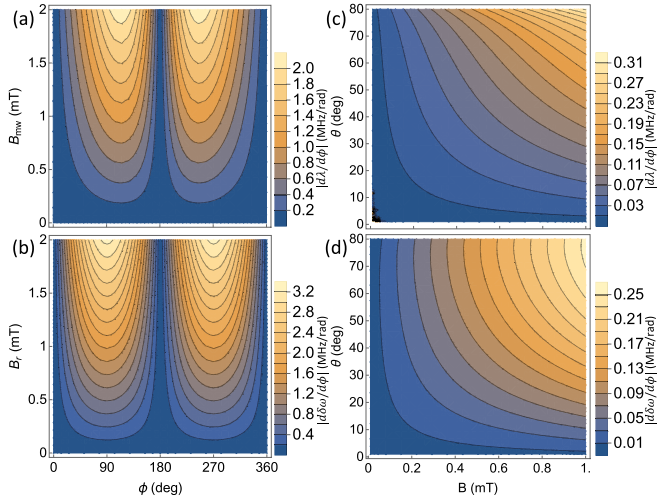


FIG. 4. (a) The derivative of the Rabi frequency $|\frac{d\lambda}{d\phi}|$ with respect to the amplitude of the microwave field B_{mw} and the azimuthal angle $\phi = \phi_s - \phi_{mw}$. (b) The derivative of the resonant frequency $|\frac{d\delta\omega}{d\phi}|$ with respect to the amplitude of the reference dc field B_r and the azimuthal angle $\phi = \phi_s - \phi_r$. Here, the polar angle of the target field θ is 40° , while $B = 8$ mT and (a) $\theta_{mw} = 20^\circ$. (c) The derivative of the Rabi frequency $|\frac{d\lambda}{d\phi}|$, with respect to the amplitude and the polar angle of the target field B . (d) The derivative of the resonant frequency $|\frac{d\delta\omega}{d\phi}|$, with respect to the amplitude and the polar angle of the target field B . Here, we use the azimuthal angle ϕ to maximize the derivative, while (c) $B_{mw} = 1.0$ mT, (d) $B_r = 1.0$ mT, and (c) $\theta_{mw} = 20^\circ$.

target field. In this case, $|\frac{d\lambda}{d\phi}|$ and $|\frac{d\delta\omega}{d\phi}|$ decrease for a smaller B_\perp , as shown in Figs. 4(c) and 4(d).

To consider the effect of the factors $c_{\tau,\Gamma}$ and $c_{\tau,\Gamma}^*$, we next obtain $\delta\phi$ by directly calculating Eq. (20) using the probability P obtained by numerically solving Eq. (22) [53]. Figure 5 shows the dependence of $\delta\phi$ on ϕ and B , respectively, corresponding to $|\frac{d\lambda}{d\phi}|$ and $|\frac{d\delta\omega}{d\phi}|$ shown in Fig. 4.

In addition, we take into account the fluorescence contrast and calculate the sensitivity for a wide range of the target magnetic field's amplitude in Fig. 6. In such cases, the uncertainty of the estimation is calculated as [8]

$$\delta\phi' = \delta\phi / C(\vec{B}), \quad (25)$$

where $C(\vec{B})$ is the fluorescence contrast that depends on the total applied dc magnetic field. The contrast $C(\vec{B})$ depends on the amplitude and the polar angle of the applied dc field and can be calculated using the seven-level classical rate equations [14]. Increasing the amplitude of the magnetic field reduces the value of $\delta\phi$, but also reduces the contrast $C(\vec{B})$. There are trade-off relationships between them, and we obtain $\delta\phi_{\min}$, the minimum values of uncertainty, as shown in Fig. 6. Let us define the detectable range as the difference between the two magnetic fields at which $\delta\phi$ becomes half of $\delta\phi_{\min}$. We calculate the detectable range as 27 mT (28 mT), 23 mT (24 mT), and 20 mT (38 mT) for $\theta = 10^\circ$, $\theta = 40^\circ$, and $\theta = 80^\circ$, respectively, by using our (conventional) method.

For simplicity, we use the same Γ for the conventional Ramsey scheme and our Rabi scheme in Figs. 5 and 6. However, in actual experiments, the coherence time of the Rabi

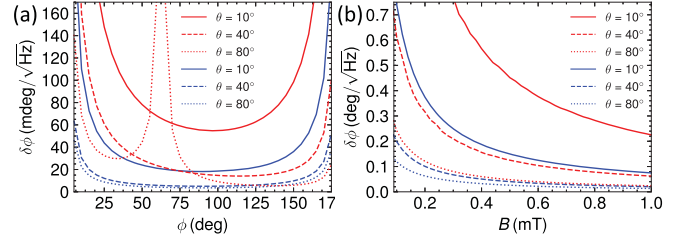


FIG. 5. (a) Uncertainty of the conventional scheme (blue lower curve) and our scheme (red upper curve) as a function of the azimuthal angles $\phi = \phi_s - \phi_r$ (blue lower curve) and $\phi = \phi_s - \phi_{mw}$ (red upper curve) for $\theta = 10^\circ$ (solid curve), $\theta = 40^\circ$ (dashed curve), and $\theta = 80^\circ$ (dotted curve). We calculate the uncertainty using Eq. (20) for $\tau = (2n - 1)\pi/2\lambda_a$ and plot the minimum (optimal) value. Here, $B = 8$ mT, $B_{mw} = 1$ mT, $B_r = 1$ mT, $\theta_{mw} = 20^\circ$, and $\Gamma = 1.0$ MHz. (b) Uncertainty of the conventional scheme (blue lower curve) and our scheme (red upper curve) as a function of the amplitude of the target field B for $\theta = 10^\circ$ (solid curve), $\theta = 40^\circ$ (dashed curve), and $\theta = 80^\circ$ (dotted curve). We calculate the uncertainty using Eq. (20) for $\tau = (2n - 1)\pi/2\lambda_a$ and plot the minimum (optimal) value. Here, we use the azimuthal angle $\phi = \phi_s - \phi_r$ ($\phi = \phi_s - \phi_{mw}$) to minimize the uncertainty of the conventional (our) scheme and fix $B_r = 2$ mT, $B_{mw} = 2$ mT, $\theta_{mw} = 10^\circ$ (solid curve), $\theta_{mw} = 20^\circ$ (dashed curve), $\theta_{mw} = 20^\circ$ (dotted curve), and $\Gamma = 1.0$ MHz.

oscillation T_{Rabi} is usually longer than that of the Ramsey measurements T_{Ramsey} [47]. The coherence time is determined by the power spectral density of the noise $S(\omega)$ [54–58]. Here, we consider an electron spin bath as a source of environmental noise, which can be modeled by the Ornstein-Uhlenbeck process [54]. The correlation function is given

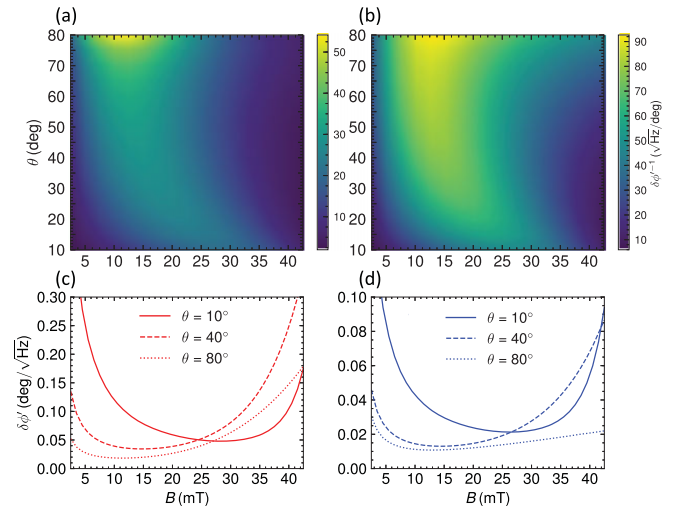


FIG. 6. Uncertainty of our scheme [panels (a) and (c)] and the conventional scheme [panels (b) and (d)] considering the effect of the fluorescence contrast $C(\vec{B})$ as a function of the amplitude and the polar angle of the target field [Eq. (25)]. Here, we have calculated the uncertainty $\delta\phi$ as in Fig. 5 and the fluorescence contrast as in Ref. [14], where we use the contrasts $C(\vec{B})$ [panels (a) and (c)] and $C(\vec{B} + \vec{B}_r)$ [panels (b) and (d)]. We use the same parameters as those in Fig. 5.

by $\int d\omega S(\omega)e^{-i\omega t} dt = b^2 e^{-|\tau/\tau_c|}$, where b is the coupling strength of the bath to the spin, and τ_c is the correlation time. The ratio between the coherence time of our method and that of the conventional method is given by $T_{\text{Rabi}}/T_{\text{Ramsey}} = S(0)/4S(\lambda)$ [54–58]. In Appendix A, we adopt this ratio and compare the performance of our method with that of the conventional method.

B. Entangled states

Here, we investigate whether a quantum strategy with entanglement outperforms the classical strategy. It is known that entanglement provides no advantage over separable states in standard Ramsey interferometry in the presence of Markovian dephasing [40]. However, Chaves *et al.* showed that entangled states could improve the sensitivity when the transversal noise is dominant, where the direction of the noise is orthogonal to that of the system Hamiltonian [59,60]. Because our scheme converts the information of the target dc field into the amplitude of the driving microwave, the NV center is mainly affected by transverse noise, which makes our scheme one of the cases where entanglement provides sensitivity improvement.

The effective Hamiltonian of the total system in this scenario is given by

$$H_{\text{eff}} = \sum_{j=1}^L \frac{1}{2} (\Omega |g\rangle_j \langle e| + \Omega^* |e\rangle_j \langle g|), \quad (26)$$

where L is the number of NV centers. By the same calculation of the master equation as in the case of separable states, we obtain the uncertainty of the estimation:

$$\delta\phi \simeq \frac{1}{c_{\tau,\Gamma,L} L \left| \frac{d\lambda}{d\phi} \right| \sqrt{T/\tau}}, \quad (27)$$

where we choose the Greenberger-Horne-Zeilinger (GHZ) state $|\psi\rangle = \frac{1}{\sqrt{2}}(|+\rangle^{\otimes L} + |-\rangle^{\otimes L})$ as an initial state and the parity operator defined by $\hat{P}_z = \bigotimes_{j=1}^L (|g\rangle_j \langle g| - |e\rangle_j \langle e|)$ as the observable, as proposed in Ref. [60] (see a detailed derivation in Appendix B).

Figure 7 plots the ratio between the uncertainty of the separable sensor and that of the entanglement sensor, up to $L = 6$, when θ is not zero. We use the same parameters as those used in Fig. 2. It should be stated that we cannot define $\delta\phi$ for $\theta = 0$. Instead, we calculate $\delta\lambda$ for $\theta = 0$ up to $L = 10$ in Fig. 7, based on an analytical solution introduced in Ref. [60], which we explain below.

It is worth mentioning that our results are a generalization of previous results. For the case of $\theta = 0^\circ$, our model corresponds to that used in Ref. [60], and the uncertainty scales as $\delta\omega = \Theta(L^{-5/6})$ in this case for a large limit of L . On the other hand, when θ is not zero, the noise operator \hat{S}_z is not completely transverse to the system Hamiltonian, deviating from the model used in Ref. [60]. In this case, our numerical simulation shows that the improvement due to entanglement decreases as θ increases. To understand this point, we use perturbation theory to solve the master equation in the interaction picture. When the effective Hamiltonian given by Eq. (26) can be analytically diagonalized, we can calculate the time

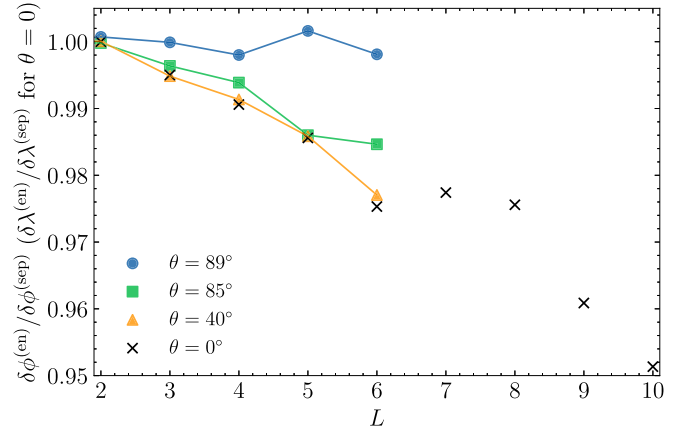


FIG. 7. Ratio between the uncertainty of the separable sensor and that of the entanglement sensor as a function of L . When θ is not zero, we numerically calculate the uncertainty using Eq. (21) for $\tau = (2n - 1)\pi/2L\lambda_a$ and select the minimum value. For $\theta = 0$, we plot the uncertainty based on an analytical solution introduced in Ref. [60]. Here, we fix $B = 8$ mT, $B_{\text{mw}} = 1$ mT, and $\Gamma = 1.0$ MHz.

evolution of $\rho_1(t)$ up to the first order as

$$\rho_1(t) \simeq \rho_1(0) - \Gamma \sum_{j=1}^L \int_0^t [\hat{S}_z^{(j)}(t), [\hat{S}_z^{(j)}(t), \rho_1(0)]], \quad (28)$$

where $\hat{S}_z^{(j)}(t) = e^{iH_{\text{eff}}t} \hat{S}_z^{(j)} e^{-iH_{\text{eff}}t}$ with $\Gamma t \ll 1$. Using this expression, we can calculate the expectation value of $\hat{P}_1 = e^{iH_{\text{eff}}t} \hat{P}_z e^{-iH_{\text{eff}}t}$.

The analytical formula for $\theta = 0^\circ$ is given up to the third order by

$$\text{Tr}[\hat{P}_1 \rho_1(t)] = 1 - \frac{1}{2} L^2 \lambda^2 t^2 + \frac{1}{6} L(3L - 2) \Gamma \lambda^2 t^3 + O(t^4), \quad (29)$$

which shows a cubic decay against time. It is shown that the entanglement strategy outperforms the classical strategy in scaling for such a cubic decay [60]. On the other hand, for $\theta = 90^\circ$, we obtain

$$\text{Tr}[\hat{P}_1 \rho_1(t)] = 1 - \frac{1}{2} L \Gamma t + O(t^2), \quad (30)$$

which shows a linear decay. It is known that an entanglement sensor does not have any advantage over separable sensors when the system exhibits a linear decay with time [40]. For $0^\circ < \theta < 90^\circ$, we cannot obtain an analytical form of $\text{Tr}[\hat{P}_1 \rho_1(t)]$, because we cannot analytically diagonalize the effective Hamiltonian. However, we can guess that the sensitivity of the entanglement sensor should be between the two, which is consistent with our numerical results.

Many theoretical and experimental studies have been carried out for the entanglement-enhanced sensing [40,42,43,61,62]. Dolde *et al.* created an entanglement between two NV centers [63], and Haruyama *et al.* demonstrated the fabrication of strongly coupled three NV centers [64]. Also, there are theoretical proposals to generate an entanglement between many NV centers [65,66]. Although an experimental demonstration of an entanglement sensor with NV centers has not been reported yet, we foresee that entanglement will play an essential role in quantum

sensing and that the use of an entanglement between multiple NV centers will be feasible in the future. As such, our results will provide practical applications in entanglement sensing.

V. CONCLUSION

In conclusion, we have proposed a scheme for vector dc magnetic-field sensing that uses microwave fields as a reference to determine the azimuthal angle of the target magnetic field. We have shown that the direction of the dc magnetic field can be measured from the Rabi frequency because the component of the resonant microwave field perpendicular to the quantization axis contributes to driving the Rabi oscillation. In addition, we investigated the potential of our method to improve the sensitivity by using entangled states and found that our sensing scheme with entanglement has sensitivity better than that of separable sensors, even under the effect of noise for most of the parameters. Our results pave the way for investigating various phenomena of materials that are sensitive to static magnetic fields.

ACKNOWLEDGMENTS

The authors gratefully acknowledge discussions with Kento Sasaki and Kensuke Kobayashi. T.I. thanks Yasutomo Ota, Guoqing Wang, Pai Peng, Changhao Li, and Paola Cappellaro for their helpful discussions. This work was supported by MEXT Q-LEAP (Grant No. JPMXS0118067395), MEXT KAKENHI (Grants No. 18H01502, No. 20H05661, and No. 22H01558), JST (Moonshot R&D) (Grant No. JPMJMS226C), and CSRN, Keio University. This work was also supported by the Leading Initiative for Excellent Young Researchers MEXT Japan; JST presto (Grant No. JPMJPR1919), Japan; and T.I. was supported by NICT Quantum Camp 2021.

APPENDIX A: DETAILED CALCULATION AND DISCUSSION ON SENSITIVITY

1. Derivation of the uncertainty of the estimation of the conventional scheme

The uncertainty of the estimation of the conventional scheme can be obtained in a way similar to that of our scheme shown in the main text. Assuming we have an approximate value of the azimuthal angle ϕ_s , we can rewrite it as $\phi_s = \phi_a + \phi'$, where ϕ_a is the approximate value and ϕ' is a small difference from the true value. The frequency shift $\delta\omega$ is then given by $\delta\omega = \delta\omega_a + \delta\omega'$, where $\delta\omega_a$ is the approximate value and $\delta\omega'$ is a small difference from the true value. We can adjust the interaction time as

$$\tau = \frac{(2n-1)\pi}{2\delta\omega_a}, \quad (\text{A1})$$

and we obtain $P \simeq (1 + \delta\omega'\tau)/2$, where we assume $\delta\omega'\tau \ll 1$. By using Eq. (20), we can calculate the uncertainty as

$$\delta\phi \simeq \frac{1}{\left| \frac{d\delta\omega}{d\phi} \right| \sqrt{T\tau}}. \quad (\text{A2})$$

The effect of decoherence can be described by the standard Lindblad-type master equation, Eq. (22). For the conventional case, the probability of projecting the state onto $|+\rangle$ can be calculated as $P = \text{Tr}[|+\rangle\langle+|\rho(t)]$. We numerically calculate

the probability P with the initial state $\rho(0) = |+\rangle\langle+|$, and we observe a linear dependence of the probability on a small $\delta\omega'$ for B_\perp between 0.1 and 10 mT. The probability P is, thus, expressed as

$$P \simeq \frac{1}{2}(1 + c_{\tau,\Gamma} \delta\omega'), \quad (\text{A3})$$

where $c_{\tau,\Gamma}$ denotes a factor calculated using numerical simulations. By substituting Eq. (A3) into Eq. (20), we obtain the uncertainty of the estimation:

$$\delta\phi \simeq \frac{1}{c_{\tau,\Gamma} \left| \frac{d\delta\omega}{d\phi} \right| \sqrt{T/\tau}}. \quad (\text{A4})$$

2. Effect of the coherence time on sensitivity

Here, we calculate the uncertainty of our scheme using a decay rate obtained from the ratio between the coherence time of our method and that of the conventional method. To compare the performance, we assume $\Gamma_{\text{Ramsey}} = 1.0$ MHz, as in the main text, and use relation $\Gamma_{\text{Ramsey}}/\Gamma_{\text{Rabi}} = T_{\text{Rabi}}/T_{\text{Ramsey}} = S(0)/4S(\lambda)$, which can be obtained by the standard technique of open quantum systems [6,54]. The power spectral density (PSD) of the noise is calculated as

$$S(\omega) = \frac{2b^2 \left(\frac{1}{\tau_c}\right)}{\left(\frac{1}{\tau_c}\right)^2 + \omega^2}, \quad (\text{A5})$$

where b is the coupling strength of the bath to the spin, and τ_c is the correlation time. As the frequency becomes smaller, the PSD tends to be larger, which makes the coherence time of the Ramsey scheme shorter. In contrast, the sensitivity of our scheme is mainly affected by the PSD whose frequency is near the Rabi frequency, thereby avoiding the effect of strong low-frequency noise. This provides the intuitive understanding of the ratio of the coherence time $T_{\text{Rabi}}/T_{\text{Ramsey}} = S(0)/4S(\lambda)$. We numerically solve Eq. (22) with $\Gamma_{\text{Rabi}} = 1.0 \times 4S(\lambda)/S(0)$ MHz and calculate the uncertainty of the estimation by using Eq. (20). We adopted a value of $\tau_c = 23 \mu\text{s}$, as estimated in Ref. [54]. Figure 8 shows the dependence of $\delta\phi$ on ϕ and B , respectively. For any ϕ and B , more than a fivefold improvement is obtained compared to the conventional scheme when we compare the results in Fig. 8 with those in Fig. 5.

APPENDIX B: DERIVATION OF THE UNCERTAINTY OF THE ESTIMATION USING ENTANGLED STATES

Let us consider an ensemble of L NV centers aligned along only one axis. In our study, we assume that the effect of the dipole-dipole interaction between the probe spins is negligible during the Rabi oscillation. This is valid, especially when the main noise source is the magnetic noise induced by nitrogen impurities and/or carbon nuclear spins in the environment [67,68].

The Hamiltonian of the total system is, thus, given by

$$H = \sum_{j=1}^L H_0^{(j)} + H_{\text{mw}}^{(j)},$$

$$H_0^{(j)} = D(\hat{S}_z^{(j)})^2 + \gamma_e B_z \hat{S}_z^{(j)} + \gamma_e B_\perp (\cos \phi_s \hat{S}_x^{(j)} + \sin \phi_s \hat{S}_y^{(j)}),$$

$$H_{\text{mw}}^{(j)} = \gamma_e \vec{B}_{\text{mw}} \cdot \vec{S}^{(j)} \cos \omega_\perp t. \quad (\text{B1})$$

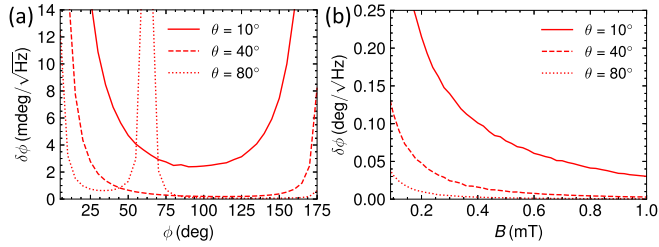


FIG. 8. (a) Uncertainty of our scheme as a function of the azimuthal angle $\phi = \phi_s - \phi_{mw}$ for $\theta = 10^\circ$ (solid curve), $\theta = 40^\circ$ (dashed curve), and $\theta = 80^\circ$ (dotted curve). We calculate the uncertainty using Eq. (20) for $\tau = (2n - 1)\pi/2\lambda_a$ and plot the minimum (optimal) value. Here, $B = 8$ mT, $B_{mw} = 1$ mT, $\theta_{mw} = 20^\circ$, and $\Gamma_{Rabi} = 1.0 \times 4S(\lambda)/S(0)$ MHz. (b) Uncertainty of our scheme as a function of the amplitude of the target field B for $\theta = 10^\circ$ (solid curve), $\theta = 40^\circ$ (dashed curve), and $\theta = 80^\circ$ (dotted curve). We calculate the uncertainty using Eq. (20) for $\tau = (2n - 1)\pi/2\lambda_a$ and plot the minimum (optimal) value. Here, we use the azimuthal angle $\phi = \phi_s - \phi_{mw}$ to minimize the uncertainty and fix $B_{mw} = 2$ mT, $\theta_{mw} = 10^\circ$ (solid curve), $\theta_{mw} = 20^\circ$ (dashed curve), $\theta_{mw} = 20^\circ$ (dotted curve), and $\Gamma_{Rabi} = 1.0 \times 4S(\lambda)/S(0)$ MHz.

We define $|g\rangle_j$ and $|e\rangle_j$ as the ground state and the first-excited state of the Hamiltonian $H_0^{(j)}$, respectively. In a rotating frame defined by $U = \exp(-i\sum_{j=1}^L H_0^{(j)}t)$, the effective Hamiltonian is

$$H_{\text{eff}} = \sum_{j=1}^L \frac{\lambda}{2} (|g\rangle_j \langle e| + |e\rangle_j \langle g|). \quad (\text{B2})$$

As an initial state, we choose the GHZ state

$$|\psi\rangle = \frac{1}{\sqrt{2}} (|+\rangle^{\otimes L} + |-\rangle^{\otimes L}), \quad (\text{B3})$$

where $|+\rangle = (|g\rangle + |e\rangle)/\sqrt{2}$ and $|-\rangle = (|g\rangle - |e\rangle)/\sqrt{2}$. As the observable, we choose the parity operator

defined by

$$\hat{P}_z = \bigotimes_{j=1}^L (|g\rangle_j \langle g| - |e\rangle_j \langle e|), \quad (\text{B4})$$

as proposed in Ref. [60]. First, let us consider the noiseless case. The expectation value of the measurement is given by $P = \cos(L\lambda t)$. Assuming that we know the approximate value of the azimuthal angle ϕ_s , we obtain $P \simeq L\lambda'\tau$ by adjusting the interaction time t , where λ' is a small difference between the approximate and true values. The uncertainty is defined as

$$\delta\phi = \frac{\sqrt{1 - P^2}}{\left| \frac{dP}{d\phi} \right| \sqrt{N}}, \quad (\text{B5})$$

and we obtain $\delta\phi \simeq \frac{1}{L \left| \frac{dP}{d\phi} \right| \sqrt{T\tau}}$ for a small λ' , where we use $\hat{P}_z^2 = \hat{I}$. Thus, we obtain $\delta\phi = \Theta(L^{-1})$, and this scaling is called the Heisenberg limit.

Second, we investigate how the decoherence affects the performance of the entanglement sensor. To account for the decoherence, we adopt the Lindblad-type master equation given by

$$\frac{d\rho(t)}{dt} = -i[H_{\text{eff}}, \rho(t)] - \sum_{j=1}^L \Gamma [\hat{S}_z^{(j)}, [\hat{S}_z^{(j)}, \rho(t)]]. \quad (\text{B6})$$

We numerically obtain the expectation value $P = \text{Tr}[\hat{P}_z \rho(t)]$ with the initial state $\rho(0) = |\psi\rangle\langle\psi|$. We observe a linear dependence of the expectation value on a small λ' for B_\perp between 0.1 and 10 mT with $\tau = (2n - 1)\pi/2L\lambda_a$. Thus, the expectation value P can be described by

$$P \simeq c_{\tau,\Gamma,L} L\lambda', \quad (\text{B7})$$

where $c_{\tau,\Gamma,L}$ denotes a factor calculated using the numerical simulations. By substituting Eq. (B7) into Eq. (B5), we obtain the uncertainty of the estimation:

$$\delta\phi \simeq \frac{1}{c_{\tau,\Gamma,L} L \left| \frac{dP}{d\phi} \right| \sqrt{T/\tau}}. \quad (\text{B8})$$

[1] F. Casola, T. van der Sar, and A. Yacoby, *Nat. Rev. Mater.* **3**, 17088 (2018).
 [2] R. Schirhagl, K. Chang, M. Loretz, and C. L. Degen, *Annu. Rev. Phys. Chem.* **65**, 83 (2014).
 [3] S. J. Bending, *Adv. Phys.* **48**, 449 (1999).
 [4] A. M. Chang, H. D. Hallen, L. Harriott, H. F. Hess, H. L. Kao, J. Kwo, R. E. Miller, R. Wolfe, J. van der Ziel, and T. Y. Chang, *Appl. Phys. Lett.* **61**, 1974 (1992).
 [5] M. Poggio and C. L. Degen, *Nanotechnology* **21**, 342001 (2010).
 [6] C. L. Degen, F. Reinhard, and P. Cappellaro, *Rev. Mod. Phys.* **89**, 035002 (2017).
 [7] J. R. Maze, P. L. Stanwix, J. S. Hodges, S. Hong, J. M. Taylor, P. Cappellaro, L. Jiang, M. V. G. Dutt, E. Togan, A. S. Zibrov, A. Yacoby, R. L. Walsworth, and M. D. Lukin, *Nature (London)* **455**, 644 (2008).

[8] J. M. Taylor, P. Cappellaro, L. Childress, L. Jiang, D. Budker, P. R. Hemmer, A. Yacoby, R. Walsworth, and M. D. Lukin, *Nat. Phys.* **4**, 810 (2008).
 [9] G. Balasubramanian, I. Y. Chan, R. Kolesov, M. Al-Hmoud, J. Tisler, C. Shin, C. Kim, A. Wojcik, P. R. Hemmer, A. Krueger, T. Hanke, A. Leitenstorfer, R. Bratschitsch, F. Jelezko, and J. Wrachtrup, *Nature (London)* **455**, 648 (2008).
 [10] M. Schaffry, E. M. Gauger, J. J. L. Morton, and S. C. Benjamin, *Phys. Rev. Lett.* **107**, 207210 (2011).
 [11] B. J. Maertz, A. P. Wijnheijmer, G. D. Fuchs, M. E. Nowakowski, and D. D. Awschalom, *Appl. Phys. Lett.* **96**, 092504 (2010).
 [12] S. Steinert, F. Dolde, P. Neumann, A. Aird, B. Naydenov, G. Balasubramanian, F. Jelezko, and J. Wrachtrup, *Rev. Sci. Instrum.* **81**, 043705 (2010).

- [13] L. M. Pham, D. L. Sage, P. L. Stanwix, T. K. Yeung, D. Glenn, A. Trifonov, P. Cappellaro, P. R. Hemmer, M. D. Lukin, H. Park, A. Yacoby, and R. L. Walsworth, *New J. Phys.* **13**, 045021 (2011).
- [14] J.-P. Tetienne, L. Rondin, P. Spinicelli, M. Chipaux, T. Debuisschert, J.-F. Roch, and V. Jacques, *New J. Phys.* **14**, 103033 (2012).
- [15] A. K. Dmitriev and A. K. Vershovskii, *J. Opt. Soc. Am. B* **33**, B1 (2016).
- [16] K. Sasaki, Y. Monnai, S. Saijo, R. Fujita, H. Watanabe, J. Ishi-Hayase, K. M. Itoh, and E. Abe, *Rev. Sci. Instrum.* **87**, 053904 (2016).
- [17] D. Le Sage, K. Arai, D. R. Glenn, S. J. DeVience, L. M. Pham, L. Rahn-Lee, M. D. Lukin, A. Yacoby, A. Komeili, and R. L. Walsworth, *Nature (London)* **496**, 486 (2013).
- [18] A. Nowodzinski, M. Chipaux, L. Toraille, V. Jacques, J.-F. Roch, and T. Debuisschert, *Microelectron. Reliab.* **55**, 1549 (2015).
- [19] J.-P. Tetienne, N. Dontschuk, D. A. Broadway, A. Stacey, D. A. Simpson, and L. C. L. Hollenberg, *Sci. Adv.* **3**, e1602429 (2017).
- [20] M. J. H. Ku, T. X. Zhou, Q. Li, Y. J. Shin, J. K. Shi, C. Burch, L. E. Anderson, A. T. Pierce, Y. Xie, A. Hamo, U. Vool, H. Zhang, F. Casola, T. Taniguchi, K. Watanabe, M. M. Fogler, P. Kim, A. Yacoby, and R. L. Walsworth, *Nature (London)* **583**, 537 (2020).
- [21] U. Vool, A. Hamo, G. Varnavides, Y. Wang, T. X. Zhou, N. Kumar, Y. Dovzhenko, Z. Qiu, C. A. C. Garcia, A. T. Pierce, J. Gooth, P. Anikeeva, C. Felser, P. Narang, and A. Yacoby, *Nat. Phys.* **17**, 1216 (2021).
- [22] J.-P. Tetienne, T. Hingant, L. J. Martínez, S. Rohart, A. Thiaville, L. H. Diez, K. Garcia, J.-P. Adam, J.-V. Kim, J.-F. Roch, I. M. Miron, G. Gaudin, L. Vila, B. Ocker, D. Ravelosona, and V. Jacques, *Nat. Commun.* **6**, 6733 (2015).
- [23] Y. Dovzhenko, F. Casola, S. Schlotter, T. X. Zhou, F. Büttner, R. L. Walsworth, G. S. D. Beach, and A. Yacoby, *Nat. Commun.* **9**, 2712 (2018).
- [24] N. F. Ramsey, *Phys. Rev.* **78**, 695 (1950).
- [25] P. Neumann, R. Kolesov, V. Jacques, J. Beck, J. Tisler, A. Batalov, L. Rogers, N. B. Manson, G. Balasubramanian, F. Jelezko, and J. Wrachtrup, *New J. Phys.* **11**, 013017 (2009).
- [26] S. Kitazawa, Y. Matsuzaki, S. Saijo, K. Kakuyanagi, S. Saito, and J. Ishi-Hayase, *Phys. Rev. A* **96**, 042115 (2017).
- [27] K. Yahata, Y. Matsuzaki, S. Saito, H. Watanabe, and J. Ishi-Hayase, *Appl. Phys. Lett.* **114**, 022404 (2019).
- [28] J. M. Schloss, J. F. Barry, M. J. Turner, and R. L. Walsworth, *Phys. Rev. Appl.* **10**, 034044 (2018).
- [29] C. Zhang, H. Yuan, N. Zhang, L. Xu, J. Zhang, B. Li, and J. Fang, *J. Phys. D: Appl. Phys.* **51**, 155102 (2018).
- [30] X.-D. Chen, F.-W. Sun, C.-L. Zou, J.-M. Cui, L.-M. Zhou, and G.-C. Guo, *Europhys. Lett.* **101**, 67003 (2013).
- [31] Y.-X. Liu, A. Ajoy, and P. Cappellaro, *Phys. Rev. Lett.* **122**, 100501 (2019).
- [32] H. Zheng, Z. Sun, G. Chatzidrosos, C. Zhang, K. Nakamura, H. Sumiya, T. Ohshima, J. Isoya, J. Wrachtrup, A. Wickenbrock, and D. Budker, *Phys. Rev. Appl.* **13**, 044023 (2020).
- [33] Z. Qiu, U. Vool, A. Hamo, and A. Yacoby, *npj Quantum Inf.* **7**, 39 (2021).
- [34] G. Wang, Y.-X. Liu, Y. Zhu, and P. Cappellaro, *Nano Lett.* **21**, 5143 (2021).
- [35] M. Tsukamoto, K. Ogawa, H. Ozawa, T. Iwasaki, M. Hatano, K. Sasaki, and K. Kobayashi, *Appl. Phys. Lett.* **118**, 264002 (2021).
- [36] G. Wang, Y.-X. Liu, J. M. Schloss, S. T. Alsid, D. A. Braje, and P. Cappellaro, *Phys. Rev. X* **12**, 021061 (2022).
- [37] L. Thiel, D. Rohner, M. Ganzhorn, P. Appel, E. Neu, B. Müller, R. Kleiner, D. Koelle, and P. Maletinsky, *Nat. Nanotechnol.* **11**, 677 (2016).
- [38] S. E. Lillie, D. A. Broadway, N. Dontschuk, S. C. Scholten, B. C. Johnson, S. Wolf, S. Rachel, L. C. L. Hollenberg, and J.-P. Tetienne, *Nano Lett.* **20**, 1855 (2020).
- [39] P. Wang, Z. Yuan, P. Huang, X. Rong, M. Wang, X. Xu, C. Duan, C. Ju, F. Shi, and J. Du, *Nat. Commun.* **6**, 6631 (2015).
- [40] S. F. Huelga, C. Macchiavello, T. Pellizzari, A. K. Ekert, M. B. Plenio, and J. I. Cirac, *Phys. Rev. Lett.* **79**, 3865 (1997).
- [41] V. Giovannetti, S. Lloyd, and L. Maccone, *Nat. Photonics* **5**, 222 (2011).
- [42] Y. Matsuzaki, S. C. Benjamin, and J. Fitzsimons, *Phys. Rev. A* **84**, 012103 (2011).
- [43] A. W. Chin, S. F. Huelga, and M. B. Plenio, *Phys. Rev. Lett.* **109**, 233601 (2012).
- [44] W. Dür, M. Skotiniotis, F. Fröwis, and B. Kraus, *Phys. Rev. Lett.* **112**, 080801 (2014).
- [45] E. M. Kessler, I. Lovchinsky, A. O. Sushkov, and M. D. Lukin, *Phys. Rev. Lett.* **112**, 150802 (2014).
- [46] T. Tanaka, P. Knott, Y. Matsuzaki, S. Dooley, H. Yamaguchi, W. J. Munro, and S. Saito, *Phys. Rev. Lett.* **115**, 170801 (2015).
- [47] J. F. Barry, J. M. Schloss, E. Bauch, M. J. Turner, C. A. Hart, L. M. Pham, and R. L. Walsworth, *Rev. Mod. Phys.* **92**, 015004 (2020).
- [48] M. W. Doherty, F. Dolde, H. Fedder, F. Jelezko, J. Wrachtrup, N. B. Manson, and L. C. L. Hollenberg, *Phys. Rev. B* **85**, 205203 (2012).
- [49] Y. Matsuzaki, H. Morishita, T. Shimooka, T. Tashima, K. Kakuyanagi, K. Semba, W. J. Munro, H. Yamaguchi, N. Mizuochi, and S. Saito, *J. Phys.: Condens. Matter* **28**, 275302 (2016).
- [50] T. Yamaguchi, Y. Matsuzaki, S. Saito, S. Saijo, H. Watanabe, N. Mizuochi, and J. Ishi-Hayase, *Jpn. J. Appl. Phys.* **58**, 100901 (2019).
- [51] B. Yang, T. Murooka, K. Mizuno, K. Kim, H. Kato, T. Makino, M. Ogura, S. Yamasaki, M. E. Schmidt, H. Mizuta, A. Yacoby, M. Hatano, and T. Iwasaki, *Phys. Rev. Appl.* **14**, 044049 (2020).
- [52] K. Hayashi, Y. Matsuzaki, T. Taniguchi, T. Shimo-Oka, I. Nakamura, S. Onoda, T. Ohshima, H. Morishita, M. Fujiwara, S. Saito, and N. Mizuochi, *Phys. Rev. Appl.* **10**, 034009 (2018).
- [53] J. Johansson, P. Nation, and F. Nori, *Comput. Phys. Commun.* **183**, 1760 (2012).
- [54] G. de Lange, Z. H. Wang, D. Ristè, V. V. Dobrovitski, and R. Hanson, *Science* **330**, 60 (2010).
- [55] F. Yan, S. Gustavsson, J. Bylander, X. Jin, F. Yoshihara, D. G. Cory, Y. Nakamura, T. P. Orlando, and W. D. Oliver, *Nat. Commun.* **4**, 2337 (2013).
- [56] M. Loretz, T. Rosskopf, and C. L. Degen, *Phys. Rev. Lett.* **110**, 017602 (2013).
- [57] G. Wang, Y.-X. Liu, and P. Cappellaro, *New J. Phys.* **22**, 123045 (2020).
- [58] G. Wang, Y.-X. Liu, and P. Cappellaro, *Phys. Rev. A* **103**, 022415 (2021).

- [59] R. Chaves, J. B. Brask, M. Markiewicz, J. Kołodyński, and A. Acín, *Phys. Rev. Lett.* **111**, 120401 (2013).
- [60] J. B. Brask, R. Chaves, and J. Kołodyński, *Phys. Rev. X* **5**, 031010 (2015).
- [61] J. A. Jones, S. D. Karlen, J. Fitzsimons, A. Ardavan, S. C. Benjamin, G. A. D. Briggs, and J. J. L. Morton, *Science* **324**, 1166 (2009).
- [62] A. Facon, E.-K. Dietsche, D. Grosso, S. Haroche, J.-M. Raimond, M. Brune, and S. Gleyzes, *Nature (London)* **535**, 262 (2016).
- [63] F. Dolde, I. Jakobi, B. Naydenov, N. Zhao, S. Pezzagna, C. Trautmann, J. Meijer, P. Neumann, F. Jelezko, and J. Wrachtrup, *Nat. Phys.* **9**, 139 (2013).
- [64] M. Haruyama, S. Onoda, T. Higuchi, W. Kada, A. Chiba, Y. Hirano, T. Teraji, R. Igarashi, S. Kawai, H. Kawarada, Y. Ishii, R. Fukuda, T. Tanii, J. Isoya, T. Ohshima, and O. Hanaizumi, *Nat. Commun.* **10**, 2664 (2019).
- [65] N. Y. Yao, L. Jiang, A. V. Gorshkov, P. C. Maurer, G. Giedke, J. I. Cirac, and M. D. Lukin, *Nat. Commun.* **3**, 800 (2012).
- [66] Y. Matsuzaki, T. Imoto, and Y. Susa, *Sci. Rep.* **12**, 14964 (2022).
- [67] E. Bauch, S. Singh, J. Lee, C. A. Hart, J. M. Schloss, M. J. Turner, J. F. Barry, L. M. Pham, N. Bar-Gill, S. F. Yelin, and R. L. Walsworth, *Phys. Rev. B* **102**, 134210 (2020).
- [68] K. Hayashi, Y. Matsuzaki, T. Ashida, S. Onoda, H. Abe, T. Ohshima, M. Hatano, T. Taniguchi, H. Morishita, M. Fujiwara, and N. Mizuochi, *J. Phys. Soc. Jpn.* **89**, 054708 (2020).